Frequency Model for EMI Study of Three-Phase Grid Connected Photovoltaic Inverter on Both DC and AC Sides

Morteza Tadbiri Nooshabadi, Jean-Luc Schanen, Shahrokh Farhangi, Hossein Iman-Eini

Frequency Model for EMI Study of Three-Phase Grid Connected Photovoltaic Inverter on Both DC and AC Sides

Morteza Tadbiri Nooshabadi
University of Tehran[1]
Univ. Grenoble Alpes[2]
m.tadbiri@ut.ac.ir
morteza.tadbiri@g2elab.grenoble-inp.fr

Jean-Luc Schanen
[2]Univ. Grenoble Alpes, CNRS
Grenoble INP, G2Elab
38000 Grenoble, France
jean-luc.schanen@grenoble-inp.fr

Shahrokh Farhangi
[1]University of Tehran
School of Electrical and Computer Engineering
Tehran, Iran
farhangi@ut.ac.ir

Hossein Iman-Eini
[1]University of Tehran
School of Electrical and Computer Engineering
Tehran, Iran
imaneini@ut.ac.ir

Abstract—This paper presents an EMC model in the frequency domain for grid connected three-phase photovoltaic inverters using the conventional Boost-Inverter topology. The aim is to estimate the EMC noises on both DC and AC sides, in order to design for instance EMI filters, or for any sensitivity analysis or optimization process. The model is developed and validated on an experimental prototype setup. The results are discussed, focusing on the contribution of each converter to the noise produced, both on the DC and AC sides by considering the impedance path of noises.

Keywords— electromagnetic interference, photovoltaic inverter, frequency model.

I. INTRODUCTION

In recent years, by significant decrease in cost of solar system (including panels and inverters), the transformer-less photovoltaic inverter is also used on a large scale [1]. Fig. 1 shows a block diagram of a grid connected transformer-less photovoltaic system. It this kind of systems, there is a potential and significant problem - the leakage current and electromagnetic interference on the AC and DC sides of the photovoltaic system without galvanic isolation [2]. This problem can disrupt the operation of the inverter and cause some undesirable faults. Adding electromagnetic interference filter on both AC and DC sides of the inverter is proposed in [3]. However, sizing those filters is time-consuming using time domain simulations, and necessitates several iterations, since the noise on both DC and AC sides are not independent. A method of designing two EMI filters simultaneously by considering the crosstalk between them was proposed in [4], which can solve this problem in the conventional design.

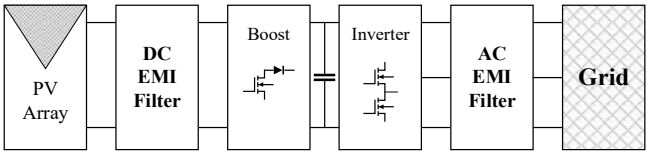

Fig. 1. The block diagram of the PV inverter system.

When high power density or lower cost is needed, filter optimization is requested. In this case, the conventional design methodology is no more sufficient and EMI models dedicated to optimization must be proposed. The frequency domain analysis [5] exhibits very low simulation times, in comparison to time domain and is well adapted to optimization approach. It replaces the switching devices by equivalent sources, and has already been used in the simple case of a DC-DC converter [6], or drive system [7]. In [8], [9], the same method is applied to a three-phase inverter with a resistive load at the output, where only one EMI filter is needed on the input side. Further studies have been carried out in [10]-[12] on the modeling of power electronics converters from an EMC point of view, with the focus on a converter. Also, in [13], a three-terminal CM EMI model for a UPS has been developed. The modeling of such researches is more restricted to a converter and an EMI filter. The purpose of this paper is to propose a frequency model for a three-phase photovoltaic inverter, composed of two cascaded converters, a Boost and a three-phase inverter. The novelty is to consider simultaneously both converters, and to account for the EMI generation on both DC and AC sides, what was not done in previous studies. The model is presented in section II, identified in section III, and validated in comparison with both experiment and time domain simulation in section IV.

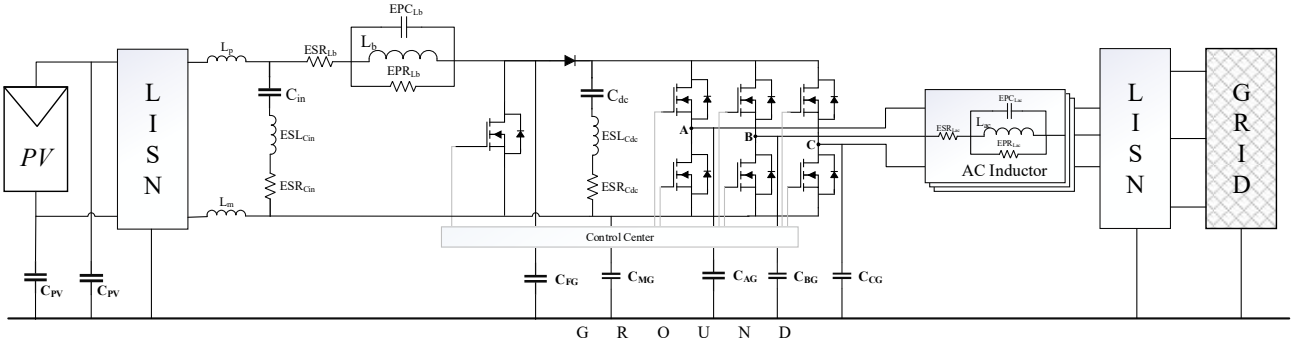

Fig. 2. The schematic of the grid connevted PV inverter system with high frequency parasitic parameters.

II. Frequency Model

First of all, since both DC and AC noise are to be considered, two LINSs (Line Impedance Stabilization Networks) are considered. No filter is used to identify the model, so the two LISN are just replacing the EMI filters boxes in Fig 1.

A circuit diagram with the parasitic parameters of the PV system is shown in Fig. 2. Each component including capacitors and inductors are modelled using high frequency model including stray elements. Common mode parasitic capacitors between the power layout and the heatsink (supposed at ground potential) are considered. The LISNs schematic and their components value are presented in Fig. 3 and Table I. Also, the used experimental LISN is shown in Fig. 4. It is worth nothing that in this study, the LISNs are used to fix the impedance in input and output and due to availability of the material for experimental validation, the DC LISN is not the 150 Ω one, which is defined in CISPR 16-1-2 or EN 55011. A 50 Ω single cell version of CISPR 16 standard is used on both DC and AC sides. This is not a serious issue, since the LISN are used to verify the model, not to measure the noise according to any kind of emission standard.

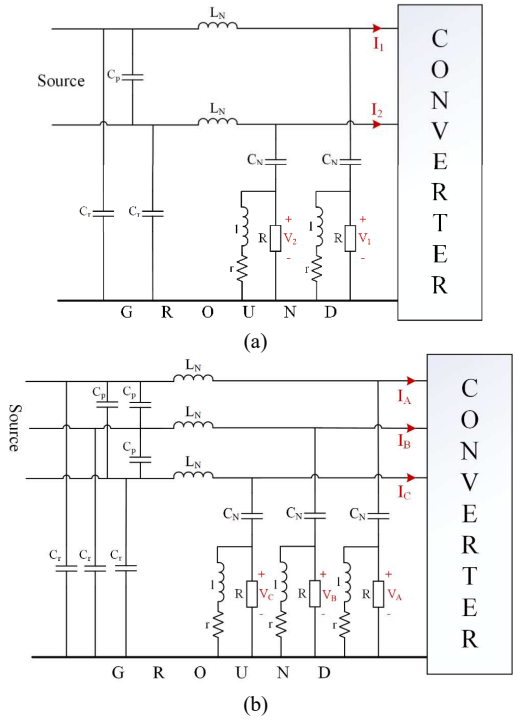

Fig. 3. Line voltage measurement in a known configuration using, (a) DC LISN on the DC side (b) three phase AC LISN on the AC side

TABLE I. LISN Parameters

L_N [µH]	250	R [Ω]	50
C_N [nF]	220	r [Ω]	5
C_r [nF]	47	l [µH]	50
C_p [µF]	1		

The disturbance voltages measured on LISN which are specified in Fig. 3 (V1, V2, VA, VB and VC) must be evaluated thanks to the frequency model.

Fig. 4. The experimental DC LISN.

To obtain the equivalent EMC model, the well-known method of equivalent sources has been chosen. It replaces the switching devices by equivalent voltage and current sources reproducing the same discontinuities [5]. Fig. 5 shows the equivalent circuit, with the voltage sources being the voltage of the MOSFETs, and the current sources being the current of the diode in the boost converter and the equivalent current of MOSFETs in the inverter. These sources can be expressed in the frequency domain which makes the solving of this circuit quite easy. The value of each source is obtained by its corresponding voltage or current spectrum which are obtained in ideal condition simulation or with either theoretical or experimental wave forms.

III. Model Identification

As it mentioned in section II, the sources in Fig. 5 (voltage and current) are obtained by transferring time domain values to frequency domain. Among mentioned methods, analytical method is the fastest one which is explained for each converter and source in the following:

A. Inverter Sources

The method is to use the PWM switching angles and a transform to convert a time signal into a frequency signal. The inverter's output voltage source is alternating at switching times, and is equal to $+V_{DC}$ when the corresponding switch (the top switch in the leg) is on and 0 when it is off. Considering a sum of signals delayed by the switching angles, the spectrum of the voltage is written as follows:

$$V_{sw,a}(h) = \frac{V_{DC}}{j\pi h}\sum_{k=1}^{m_f}\left(e^{-jh\theta(k)} - e^{-jh\theta'(k)}\right) \quad (1)$$

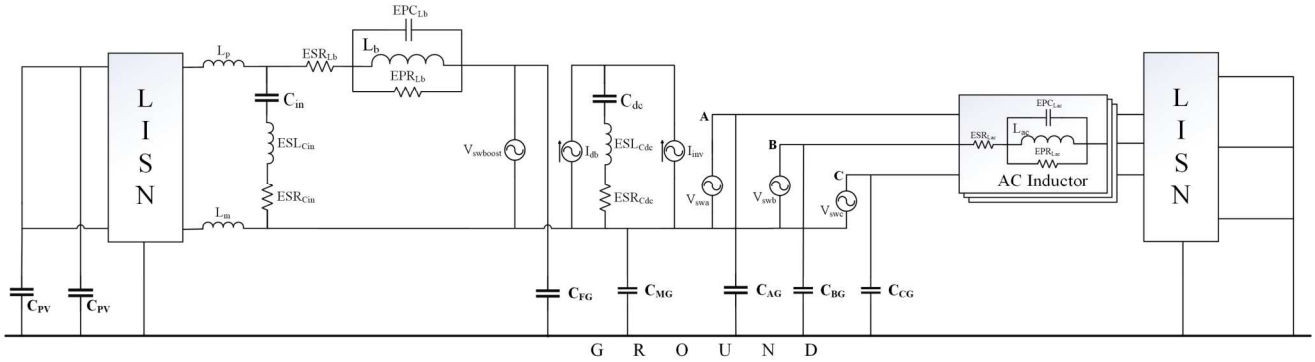

Fig. 5. Equivalent circuit for EMC studies.

With h, the harmonic order, θ, the closing angle and θ', the opening angle as (2) and (3).

$$\theta(k) = \frac{(2k-1)T_{sw}\omega_0}{2} - \frac{T_{sw}\omega_0}{2}\frac{1+m_a\,sin\left(\omega_0\frac{2k-1}{2}T_{sw}\right)}{2} \quad (2)$$

$$\theta'(k) = \frac{(2k-1)T_{sw}\omega_0}{2} + \frac{T_{sw}\omega_0}{2}\frac{1+m_a\,sin\left(\omega_0\frac{2k-1}{2}T_{sw}\right)}{2} \quad (3)$$

Where m_f, ma, T_{sw} and ω_0 are frequency index, modulation index, inverter switching frequency and grid frequency respectively. This is worth nothing the other voltage sources of the inverter have the same spectrum with only 120 degrees of phase shift.

Using the same method, the switch current is obtained by multiplying the line current in time domain by the switching pattern and finally, the input current of the inverter is obtained by summing the current of switches in three different legs as proposed in [14].

B. Boost Converter Sources

The value of voltage source of boost converter is obtained by the spectrum of voltage of boost converter switch as (4):

$$V_{sw,boost}(h) = \frac{V_{DC}}{j\pi h}(1 - e^{-j2\pi h D_b}) \quad (4)$$

Where D_b is the duty cycle of the boost converter. The current source of the boost converter is representative of the diode current in the converter that carries the ripple current in addition to the step one.

$$i_{out,boost}(h) = \frac{2}{T_{sw,b}}\int_{D_bT_{sw,b}}^{T_{sw,b}}\left[I_{in} + \frac{\Delta I_{Lb}}{2} - \frac{\Delta I_{Lb}}{(1-D_b)T_{sw,b}}(\tau - D_bT_{sw,b})\right]e^{-jh\frac{2\pi}{T_{sw,b}}}d\tau \quad (5)$$

Besides the analytical method, the spectrum can also be obtained by a FFT of a time domain simulation, or a FFT of measured signals. As an illustration, the spectrum of $V_{sw,boost}$ for the case study for three different method is shown in Fig. 6. The results match very well till 3 MHz, what is sufficient in the objective of filter design, which are very often governed by the low frequency part of the EMI spectrum. Obviously, the model would be the most accurate with sources modeled by experimental data, but due to the number of sources (six sources) and the requirement of 50 Hz harmonic accuracy for the spectrum, a large amount of data with a high sampling rate is needed. So, the measurement way is in practice very difficult or even impossible. In addition, because of the effect of the phase shift on the system, the sources must have the same reference and be considered simultaneously, what leads to another difficulty. Analytical method or FFT on simulated waveforms are therefore to be used. For practical reasons, simulation data for identifying the sources have been chosen.

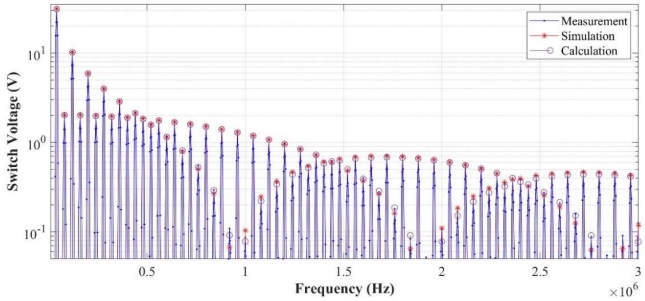

Fig. 6. Comparison between measurement, simulation and analytical methods in voltage source of the boost converter.

Other components that must be identified are the passive elements and their stray behavior. The value of these components is measured and listed in Table II. In addition, C_{pv} is assumed 100 pF as in [15]. However, due to the ability of LISNs in fixing the impedance, this arbitrary value does not impact significantly the results, since it is before the stabilization network.

TABLE II. CONVERTER MODEL PARAMETERS

Lp [nH]	500	**Lm [nH]**	500
C_{in} [µF]	163	**C_{dc} [µF]**	163
Esl_{Cin} [nH]	192	**Esl_{Cdc} [nH]**	192
Esr_{Cin} [mΩ]	60	**Esr_{Cdc} [mΩ]**	60
L_b [µH]	435	**L_{ac} [mH]**	1.05
Epr_{Lb} [kΩ]	94	**Epr_{Lac} [kΩ]**	111
Epc_{Lb} [pF]	82	**Epc_{Lac} [pF]**	258
Esr_{Lb} [mΩ]	57	**Esr_{Lac} [mΩ]**	38

Four modules (one module in the boost converter and three in the inverter) are used in the system. As shown in Fig. 7, each module consists in a leg and a 470nF decoupling capacitor. The top MOSFET in the boost converter module is not driven and only its diode is used. To identify the stray capacitance of the power modules the voltage across the decoupling capacitor is supposed to be fixed by the DC link voltage and so these two points are considered short circuited during identification. The modified power module schematic is shown in Fig. 8. Because of existence of semiconductor and decoupling capacitors, the measurement of each capacitor separately is not possible but the total capacitance is available by shorting the P and M points and measuring these points through the ground. In this case, the C_{oss} is much higher than stray capacitances and does not affect on their identification.

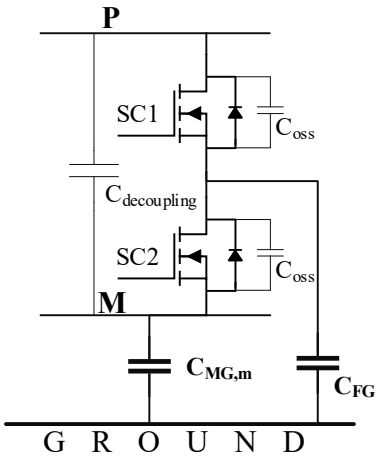

Fig. 7. Power module schematic.

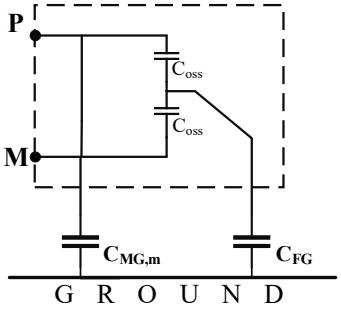

Fig. 8. Modified power module schematic.

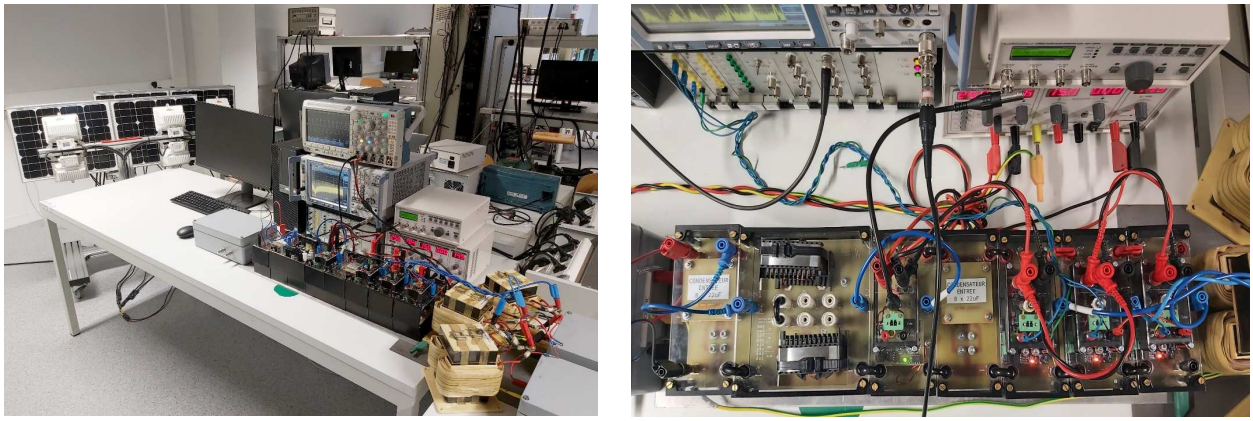

Fig. 10. Experimental prototype setup for EMC study.

The measured capacitance is equal to:

$$C_{measured} = C_{MG,m} + C_{FG} = 100\ pF \quad (6)$$

The layout of the module is shown in Fig. 9. The main contribution of capacitance is the drain of the MOSFET which is connected to the back side of the TO-247 package. The capacitances from the drain to the heatsink are dedicated to stray capacitance. Based on the layout symmetry of the modules, the value of each capacitance is considered equal and 50 pF.

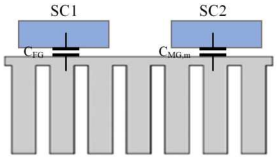

Fig. 9. Layout of the power module.

As the same modules are used for the system, the stray capacitance for other modules are considered identical. The $C_{MG,m}$ of each module is in parallel with the others. So, the total C_{MG} is equal to four times that of each module and 200 pF. The value of stray capacitances of power modules are listed at Table III.

TABLE III. POWER MODULES STRAY ELEMEMTNS

C_{MG} [pF]	200
C_{FG}, C_{AG}, C_{BG}, C_{CG} [pF]	50

IV. EXPERIMENTAL RESULTS

The configuration of the experimental test prototype is shown in Fig. 10. This is a very low power prototype just for demonstration purpose, using very low voltage. The input voltage is considered to be 25V and the boost converter operates with a duty cycle of 0.5 with a 35 kHz switching frequency. The 50W three-phase inverter switches at 40 kHz and the modulation index of the SPWM (Sine Pulse Width Modulation) control is 0.8. The two converters are assumed to operate at different switching frequencies to distinguish between noise generated by the two converters on each DC and AC sides. The reference voltage and output AC current are shown in Fig. 11, a simple resistive load on the AC side replacing the grid.

The disturbance voltages are measured and compared with both time domain simulation and the frequency model. The frequency range used for comparison is focused on the low frequency part of the spectrum (below 3MHz), since it is the most impacting range for EMI filter design regarding weight,

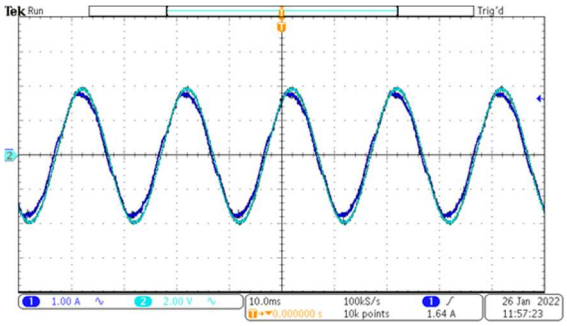

Fig. 11. The reference voltage and output line current.

volume or cost. Higher frequencies are linked with stray elements and layout. Fig. 12 and Fig. 13 show the disturbance voltages on the DC and AC side respectively. As presented, the model fits the measured noises as well as the simulation results and reproduces the effect of different switching frequencies of the two converters (the peaks amplitude are matching well). It is worth noting that the EMI noise on the DC side is not only due to the boost converter, but also contains part of the three-phase inverter (This can be clearly identified since the two switching frequencies have been chosen different). However, in the considered specific case, it is found that the noise created by the inverter is dominant in the AC side, and much larger than boost converter in the DC side. This is due to the different impedances in the DC and AC noise path where the AC noise passes through both LISNs and the DC noise passes through almost the DC LISN.

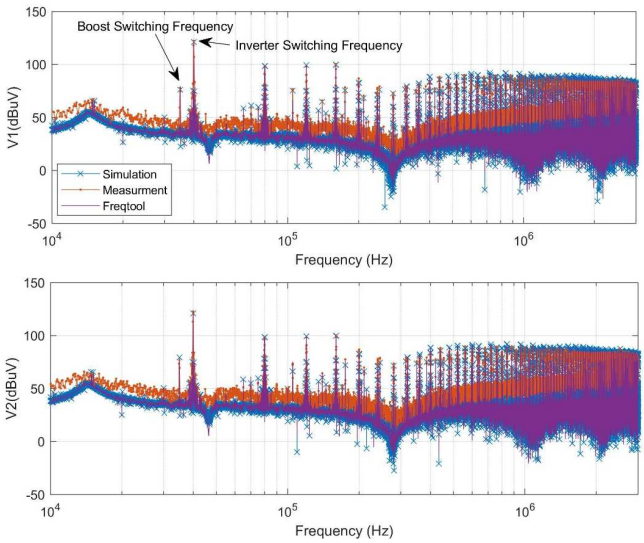

Fig. 12. DC side disturbance voltages.

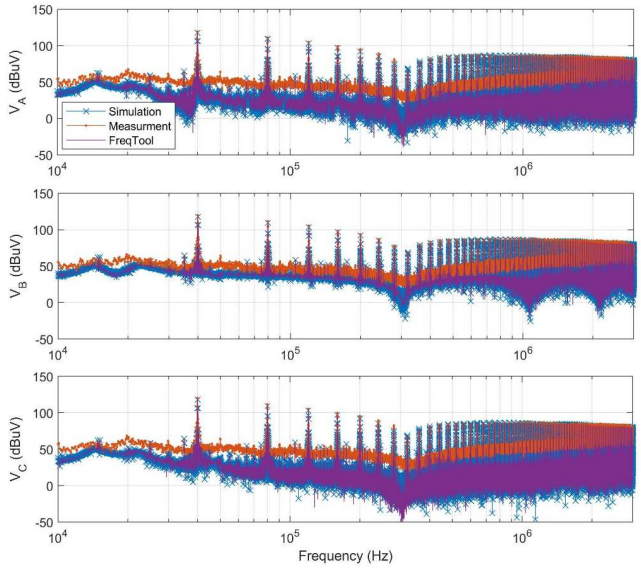

Fig. 13. AC side disturbance voltages. Simulation is obtained from a time domain simulation, Freqtool is the proposed frequency model.

As it is clear in Fig. 5, the current sources do not have any effect on measured noises on both sides, since they are looping in the DC capacitor. This is of course a first order approximation, but in the frequency range of interest, it is valid. The noises are thus generated by the voltage sources only. Based on superposition principle, the equivalent circuit in each voltage source consideration on DC and AC sides thanks to common mode are shown in Fig. 14 and Fig. 15 respectively. The $V_{cm,ac}$ is the representative of the common mode voltage which is generated by the inverter.

$$V_{cm,ac} = \frac{V_{swa}+V_{swb}+V_{swc}}{3} \quad (7)$$

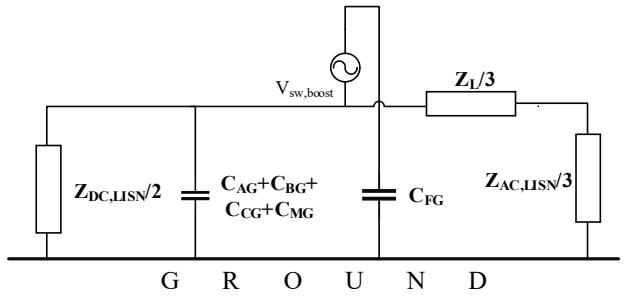

Fig. 14. The equivalent circuit of the system in the case of the DC voltage sources consideration.

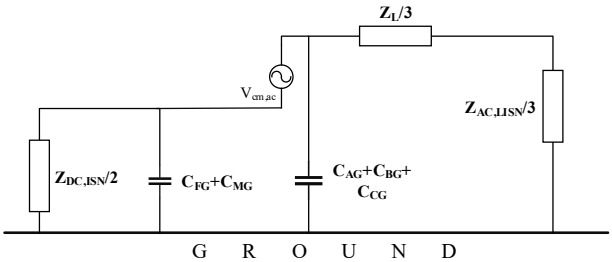

Fig. 15. The equivalent circuit of the system in the case of AC voltage sources consideration.

As it is clear in the equivalent circuits, the noises can pass through both DC and AC sides. In Fig.14, the generated noise after passing through C_{PG} is divided into two paths in the DC and AC sides. The amount of divided noise depends on the impedance path where the AC impedance is higher than DC one in the frequency range of interest as presented in Fig. 16.

Thus, most of the DC noise passes through the DC side and has no significant effect on the AC side. Unlike the DC side, the generated noise by the inverter does not pass-through stray capacitances. This is illustrated in Fig. 17, where Z_c, which represents the impedance of $C_{AG}+C_{BG}+C_{CG}$ by (8), is higher than the impedance of the line inductor and AC LISN path and most of the noise passes through the inductor and AC LISN path. Also, from Fig. 15, it is deduced that the majority of noise passes through the DC LISN.

$$Z_C(f) = \frac{1}{j.2\pi f.(C_{AG}+C_{BG}+C_{CG})} \quad (8)$$

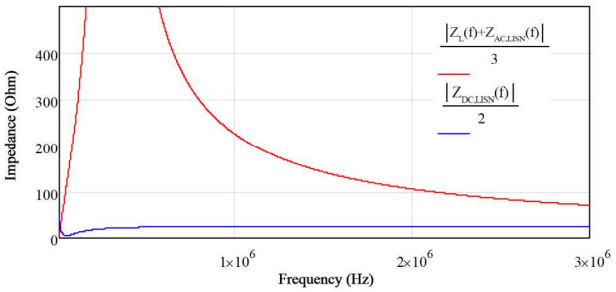

Fig. 16. Impedance curve in different paths in the case of DC voltage source consideration.

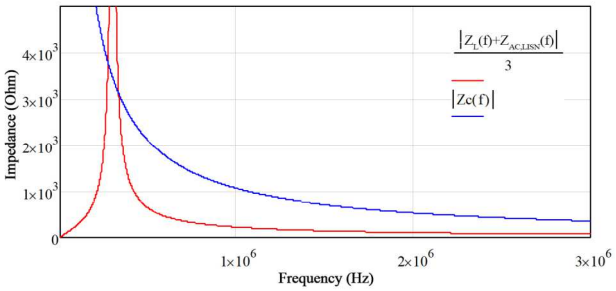

Fig. 17. Impedance curve in different paths in the case of AC voltage source consideration.

On the other hand, due to the existence of C_{PG} in the noise path, the impedance in the noise path of the boost converter (Fig. 14) is higher than that of the inverter (Fig. 15). Therefore, regardless of the value of voltage sources (even though the envelope of the boost converter voltage source is higher than that in the inverter (Fig. 18)), the noise generated by the inverter is greater than that of the boost converter, and since most of the noise generated by the inverter passes through the DC side, it is dominant in the DC side.

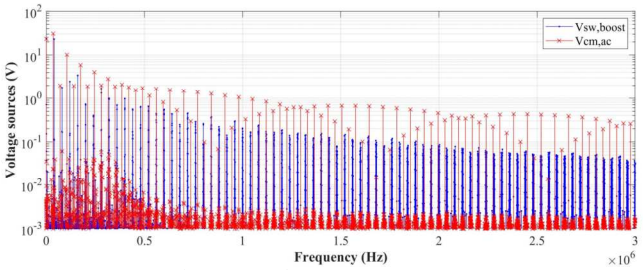

Fig. 18. Voltage sources spectrum.

V. CONCLUSIONS

In this paper, the frequency model for a three-phase photovoltaic system with two converters at different switching frequencies is explored. The identification methods of the sources and stray elements is explained. The results are then compared to experimental and time domain simulation. The contribution of each converter to the produced noise is discussed and shown by impedance path of noises.

REFERENCES

[1] REN21, "RENEWABLES 2021 GLOBAL STATUS REPORT," 2021. Accessed: Jan. 31, 2022. [Online]. Available: https://www.ren21.net/reports/global-status-report/

[2] D. Meneses, F. Blaabjerg, Ó. García, and J. A. Cobos, "Review and Comparison of Step-Up Transformerless Topologies for Photovoltaic AC-Module Application," IEEE Transactions on Power Electronics, vol. 28, no. 6, pp. 2649–2663, Jun. 2013, doi: 10.1109/TPEL.2012.2227820.

[3] X. Zhang, D. Boroyevich, P. Mattavelli, J. Xue, and F. Wang, "EMI filter design and optimization for both AC and DC side in a DC-fed motor drive system," in 2013 Twenty-Eighth Annual IEEE Applied Power Electronics Conference and Exposition (APEC), Mar. 2013, pp. 597–603. doi: 10.1109/APEC.2013.6520271.

[4] J. Zhang, W. Chen, Y. Sha, Y. Han, and X. Yang, "EMI filter analysis for transformer-less photovoltaic inverter," 2016 IEEE 8th International Power Electronics and Motion Control Conference, IPEMC-ECCE Asia 2016, pp. 1556–1560, 2016, doi: 10.1109/IPEMC.2016.7512523.

[5] B. Revol, J. Roudet, J.-L. Schanen, and P. Loizelet, "EMI Study of Three-Phase Inverter-Fed Motor Drives," IEEE Transactions on Industry Applications, vol. 47, no. 1, pp. 223–231, Jan. 2011, doi: 10.1109/TIA.2010.2091193.

[6] M. Delhommais, G. Dadanema, Y. Avenas, F. Costa, J. L. Schanen, and C. Vollaire, "Design by optimization of power electronics converter including EMC constraints," in 2016 International Symposium on Electromagnetic Compatibility - EMC EUROPE, Sep. 2016, pp. 182–187. doi: 10.1109/EMCEurope.2016.7739226.

[7] B. Touré, J.-L. Schanen, L. Gerbaud, T. Meynard, J. Roudet, and R. Ruelland, "EMC Modeling of Drives for Aircraft Applications: Modeling Process, EMI Filter Optimization, and Technological Choice," IEEE Transactions on Power Electronics, vol. 28, no. 3, pp. 1145–1156, Mar. 2013, doi: 10.1109/TPEL.2012.2207128.

[8] Y. Xiang, X. Pei, W. Zhou, Y. Kang, and H. Wang, "A Fast and Precise Method for Modeling EMI Source in Two-Level Three-Phase Converter," IEEE Transactions on Power Electronics, vol. 34, no. 11, pp. 10650–10664, Nov. 2019, doi: 10.1109/TPEL.2019.2891120.

[9] W. Zhou, X. Pei, Y. Xiang, and Y. Kang, "A New EMI Modeling Method for Mixed-Mode Noise Analysis in Three-Phase Inverter System," IEEE Access, vol. 8, pp. 71535–71547, 2020, doi: 10.1109/ACCESS.2020.2983084.

[10] D. O. Boillat, F. Krismer, and J. W. Kolar, "EMI Filter Volume Minimization of a Three-Phase, Three-Level T-Type PWM Converter System," IEEE Trans. Power Electron., vol. 32, no. 4, pp. 2473–2480, Apr. 2017, doi: 10.1109/TPEL.2016.2617085.

[11] Z. Shen, D. Jiang, T. Zou, and R. Qu, "Dual-Segment Three-Phase PMSM with Dual Inverters for Leakage Current and Common-Mode EMI Reduction," IEEE Trans. Power Electron., vol. 34, no. 6, pp. 5606–5619, 2019, doi: 10.1109/TPEL.2018.2866338.

[12] A. Nidhal, C. Dhia, and S. Lassad, "Modelling of conducted EMI generated by a three-phase PWM rectifier," in 2017 International Conference on Green Energy Conversion Systems (GECS), Mar. 2017, pp. 1–4. doi: 10.1109/GECS.2017.8066163.

[13] S. Ohn et al., "Three-terminal common-mode EMI model for EMI generation, propagation, and mitigation in a full-sic three-phase ups module," IEEE Transactions on Power Electronics, vol. 34, no. 9, pp. 8599–8612, Sep. 2019, doi: 10.1109/TPEL.2018.2883714.

[14] A. Voldoire, J. L. Schanen, J. P. Ferrieux, C. Gautier, and C. Saber, "Analytical calculation of dc-link current for N-Interleaved 3-Phase PWM inverters considering AC current ripple," 2019 21st European Conference on Power Electronics and Applications, EPE 2019 ECCE Europe, p. P.1-P.10, 2019, doi: 10.23919/EPE.2019.8915183.

[15] B. Yang, W. Li, Y. Gu, W. Cui, and X. He, "Improved Transformerless Inverter With Common-Mode Leakage Current Elimination for a Photovoltaic Grid-Connected Power System," IEEE Transactions on Power Electronics, vol. 27, no. 2, pp. 752–762, Feb. 2012, doi: 10.1109/TPEL.2011.2160359.